Atomistic model of xenon gas bubble re-solution rate due to thermal spike in uranium oxide

Wahyu Setyawan, Michael W. D. Cooper, Kenneth J. Roche, Richard J. Kurtz, Blas P. Uberuaga, David A. Andersson, and Brian D. Wirth

Citation: Journal of Applied Physics **124**, 075107 (2018); doi: 10.1063/1.5042770
View online: https://doi.org/10.1063/1.5042770
View Table of Contents: http://aip.scitation.org/toc/jap/124/7
Published by the American Institute of Physics

Atomistic model of xenon gas bubble re-solution rate due to thermal spike in uranium oxide

Wahyu Setyawan,[1,a)] Michael W. D. Cooper,[2] Kenneth J. Roche,[1] Richard J. Kurtz,[1] Blas P. Uberuaga,[2] David A. Andersson,[2] and Brian D. Wirth[3]
[1]*Pacific Northwest National Laboratory, Richland, Washington 99352, USA*
[2]*Los Alamos National Laboratory, Los Alamos, New Mexico 87545, USA*
[3]*University of Tennessee, Knoxville, Tennessee 37996, USA*

(Received 4 June 2018; accepted 1 August 2018; published online 21 August 2018)

Atomistic simulations are performed to study the response of Xe gas bubbles in UO_2 to ionizing fission products through the thermal spike approximation. A portion of the total electronic stopping power (S_e) is taken as the thermal spike energy through a ratio variable ζ. The thermal spike energy causes extreme melting within the fission track cylindrical region. Molecular dynamics is employed to quantify the probability of a Xe gas atom to be re-solved (re-dissolved) back into the UO_2 matrix. Subsequently, a re-solution model is developed and parametrized as a function of bubble radius (R), off-centered distance (r), and thermal spike energy (ζS_e). The off-centered distance measures the shift of the thermal spike axis from the bubble center. To evaluate the re-solution model, independent fission product yield of U-235 fission due to thermal neutrons (0.0253 eV), taken from the JEFF-3.3 database, is used. The kinetic energy of the fission products is taken from the EXFOR database. Subsequently, the decay of S_e over distance for each fission product is simulated. Finally, the evaluated re-solution rate (re-solution probability per second) is presented as a function of bubble radius for a range of ζ. *Published by AIP Publishing.*
https://doi.org/10.1063/1.5042770

I. INTRODUCTION

In uranium dioxide (UO_2) nuclear fuel, xenon isotopes are the main gaseous fission products at the end of the various decay chains.[1] Accumulation of fission gas atoms increases the risk of the release of the radioactive gas atoms to the environment and/or increases the pressure in the fuel rod that may lead to mechanical failures.[2–10] For safety and economic efficiency, it is important to be able to accurately predict the fate of the fission gas atoms. Xenon atoms have vanishingly low solubilities in UO_2 and readily form bubbles.[11–17] The distribution of these bubbles[6,18–21] directly relates to the pressure in the fuel rod. On the one hand, bubbles grow by absorbing gas atoms via diffusion[3,9,19,22–30] or by bubble coalescence.[6,31] On the other hand, energetic fission products interact with gas atoms in the bubbles, leading to the re-introduction of dissolved gas back to the UO_2 matrix, a process known as gas bubble re-solution.[32–38] The re-solution rate is a parameter that directly enters the effective gas diffusion coefficient employed in fission gas release models.[5,6,8,9,39–45] Among the first experimental indications of bubble re-solution in UO_2 is the work by Whapham[18] that showed that small (2.5-nm radius) bubbles disappeared when the sample was re-irradiated with fission products at 100 °C. Evidently, the distribution of bubbles is governed by a dynamic balance between the above two competing processes, which in turn depend on, among other factors, fission rate density, fission dose, and temperature.

Two mechanisms of re-solution have been introduced based on how the energetic fission products dissipate their energy as they travel through the material. The first one is via atomic collision cascades (i.e., due to the nuclear stopping).[32,46] The other is due to the electronic stopping, which raises the local temperature within the fission tracks to a value that is often much higher than the melting temperature of the UO_2.[19,33,47] The first mechanism has been termed homogeneous re-solution while the latter heterogeneous re-solution. However, the physical meaning of the terminologies is somewhat unclear. The atomistic processes involved in both mechanisms occur in the pico- and nano-second time scales and hence cannot be readily explored with experimental methods but are well-suited for atomistic simulations.

In 2009, Schwen *et al.*[35] investigated the homogeneous re-solution of a 1-nm radius Xe bubble at 1600 K using a combination of binary collision and molecular dynamics (MD) methods. First, using a simulation box containing 7.4×10^{-4} bubbles/nm^3 and Xe density in the bubbles of 20 atoms/nm^3, binary collision simulations were performed to obtain the energy distribution of Xe primary recoils (Xe atoms directly scattered by the energetic fission products) when the system is subjected to various fission products with different atomic numbers. The identity and kinetic energy of the fission products were randomly sampled from the kinetic energy distribution of U-233 fission products from Ref. 48. The Xe primary recoils were subsequently used to initiate displacement cascades using MD. The simulations resulted in about 5 re-solved atoms per fission product. A re-solution rate (the probability of a gas atom to be re-solved per second) was then evaluated for a typical fission rate density of

a)Author to whom correspondence should be addressed: wahyu.setyawan@pnnl.gov

10^{-8}/nm^3 s corresponding to the fission rate density of a 2.5%-enriched UO_2 fuel.[33] The evaluated homogeneous re-solution rate was $b_{hom} = 3 \times 10^{-6}$/s.[35]

The re-solution rate calculated by Schwen is about 50× lower than calculated using an analytical model by Nelson[32] and two orders of magnitude lower than the empirically fitted value by Lösönen (3×10^{-4}/s).[7] Note that Lösönen's empirical value represents a total re-solution rate, i.e., it is not mechanism-specific. Three years later, Govers *et al.* performed MD simulations of homogeneous re-solution using larger bubbles (radii of 2 and 2.5 nm) at 1000 K.[37] Gas densities from 7.6 to 22.9 Xe/nm^3 were investigated. A uranium atom (5.8 nm from the center of the bubbles) was used as a primary knock-on atom (PKA). Using PKA energies ranging from 10 to 50 keV, Govers and co-workers found that out of 63 simulations, the largest number of re-solved atoms was only three, which occurred in only two simulations. Due to this extremely low probability, the authors suggested that the homogeneous re-solution in their simulations was negligible. Up to this point, the simulations by Schwen *et al.* and Govers *et al.* suggest that homogeneous re-solution alone cannot fully account for Lösönen's empirical value.

In 2010, Huang *et al.*[36] performed MD simulations to explore if local heating in the heterogeneous re-solution mechanism can produce more extensive re-solution than collision cascades. The local heating due to electronic stopping was modeled via a thermal spike approximation. In this approximation, a portion of the energy that is originally deposited to the electrons is transferred to the lattice as thermal energy (thermal spike energy). The thermal spike energy is then distributed to atoms within a fission track. A cylindrical region is used to model the fission track. Electronic stopping powers of $S_e = 32.8$, 47.0, and 55.4 keV/nm were investigated. The radial temperature profile in the thermal spike region was initialized by creating several coaxial shells and rescaling the velocity of atoms in each shell. The evolution of the temperature profile was compared to that obtained from solving coupled heat diffusion equations between the electronic system and the lattice [two-temperature (2T) model].[49,50] The comparison allows for calibrating the initial temperature profile used in the MD simulations as well as for estimating the thermal spike energy. Since the thermal spike energy represents the portion of S_e that effectively causes the re-solution, it is referred to as the effective electronic stopping power $S_{e,eff}$. In Huang's simulations, the system was equilibrated at 300 K before the thermal spike was introduced. A 1-nm radius bubble, containing a xenon density of 20 Xe/nm^3, was used to study the re-solution. Two geometries were investigated: (1) on-centered, where the axis of the thermal spike passed the bubble center, and (2) tangential, where it passes tangentially along the bubble surface. The on-centered simulations resulted in 6.3% and 14.6% re-solved atoms with 47.0 and 55.4 keV/nm, respectively. The values from the tangential thermal spikes were lower, at 3.2% and 12.0%, respectively. In both cases, no re-solution was observed with $S_e = 32.8$ keV/nm. The results suggest that no re-solution is expected from fission products in UO_2 since their electronic stopping powers do not exceed 22 keV/nm.[51]

Two years later, Govers *et al.* performed thermal spike simulations that included bubbles with different sizes and gas densities.[37] Unlike Huang *et al.*, Govers *et al.* directly specified $S_{e,eff}$ as an input parameter in the simulations. The thermal spike energy was initially distributed uniformly within a 4-nm radius cylinder. The system was equilibrated at 1000 K before the thermal spike was introduced. Bubbles with radii of 0.8, 1.2, 1.5, 2, and 2.5 nm and gas densities ranging from 8 to 23 Xe/nm^3 were subjected to a thermal spike with $S_{e,eff}$ ranging from 10 to 42 keV/nm. The simulations showed that re-solution occurred with $S_{e,eff} \geq 15$ keV/nm. Analyses of the re-solution as a function of bubble size and gas density were not presented, presumably because of the lack of any clear trend on the dependencies. Hence, all data points were fitted with a single linear model

$$N_{res} = \alpha(S_{e,eff} - S_{e,c}), \tag{1}$$

where N_{res} is the number of re-solved atoms, $\alpha = 2.7$ atoms/(keV/nm), and $S_{e,c} = 13.2$ keV/nm is the fitted critical $S_{e,eff}$ above which re-solution can occur.

To relate the thermal spike energy to the total electronic stopping power of fission products, which is typically on the order of 18 to 22 keV/nm for the heavy and light fission products,[51] Govers *et al.* performed a parametric study by varying $S_{e,eff}$ and observed that dislocation loops and disoriented nanodomains start to form in pure UO_2 at $S_{e,eff} = 16$ keV/nm. The dislocation loops have a Burgers vector along [110], similar to those observed after low-dose fission product irradiations by Soullard.[37,52] This comparison suggests that about 16/22 = 73% to 16/18 = 89% of the total electronic stopping power should be taken to model thermal spikes in MD simulations. Let us denote this ratio as $\zeta = S_{e,eff}/S_e$. To compare with the results of Huang *et al.*, Govers *et al.* estimated (based on the data provided by Huang *et al.*) that the 2T model imposes values of ζ between 0.3 and 0.5. Using this range of ζ, the $S_e = 32.8$ keV/nm in Huang's work (in which no re-solution occurred) corresponds to $S_{e,eff}$ between 9.8 and 16.4 keV/nm, which is in close agreement with the $S_{e,c}$ value in Govers' work (13.2 keV/nm).

While Govers *et al.* have performed many thermal spike simulations, only on-centered thermal spikes were investigated. In addition, a careful analysis of the re-solution dependence on bubble size and pressure was missing. In this paper, we report the results of our thermal spike simulations, which reveal a systematic dependence of the re-solution on the bubble size, fission product track-bubble interaction geometry (e.g., off-centered distance between the axis of the thermal spike and the bubble center), and $S_{e,eff}$. These results allow us to construct an updated model of heterogeneous re-solution rate, which incorporates the dependencies on the above parameters. In addition, we will evaluate this model by using a realistic distribution of fission products, accounting for decay of the electronic stopping power as a function of distance for each fission product.

II. METHODS

In 2014, Cooper *et al.* reported a consistent set of empirical potentials to describe pure actinide oxides (AcO_2 where

Ac = Am, Ce, Cm, Np, Th, Pu, and U).[53] These potentials can reproduce a range of thermo-physical properties (lattice parameter, thermal expansion coefficient, elastic constants, bulk modulus, enthalpy of formation, and specific heat) between 300 K and 3000 K. Another property that is particularly pertinent to thermal spike simulations is the melting behavior. In fact, the Cooper potential predicts the melting temperature of UO_2 to be 3050 ± 50 K, in excellent agreement with the experimental value (3147 ± 20 K).[54] For comparison, the 2003 Morelon potential[55] that is used in the re-solution simulations of Schwen, Huang, and Govers predicts 3500 ± 65 K as calculated by Govers[56] and 3300 K as calculated by Schwen.[35] Readers interested in a more complete description of the Cooper potential properties and comparison with the earlier potentials are referred to Refs. 53, 56, and 57. The Cooper potentials for the pure actinide oxides employ the same oxygen-oxygen interaction, allowing a more consistent extension to mixed oxide potentials, which are subsequently published in Refs. 58 and 59. In 2016, Cooper *et al.* added the Xe and Kr interactions in CeO_2, ThO_2, UO_2, and PuO_2.[60] The interactions of Xe and Kr in those oxides were fit by matching to density functional theory (DFT) forces in various configurations at temperatures from 300 K to 5000 K. The potentials were then validated against the literature and DFT defect trapping energies for Xe and Kr in those oxides. The above sets of Cooper potentials provide a powerful tool to explore various pure and mixed oxide fuels. Therefore, we use the Cooper potential in this study. The Xe-Xe, Xe-Kr, and Kr-Kr interactions used in the Cooper potentials were subsets of the noble gas potentials developed by Tang-Toennies.[61]

The thermal spike simulations are performed with the LAMMPS code[62] in an orthogonal box where the axis of the thermal spike and the [100] direction of the UO_2 crystal are oriented along x. The box represents a $150 \times 60 \times 60$ supercell (approximately $81.9 \times 32.7 \times 32.7\,nm^3$) containing about 6.5 million atoms. There are five collinear Xe bubbles in the box equally spaced along x, i.e., 16.4 nm center-center distance. Full periodic boundaries are applied. The system is initially equilibrated at 600 K and zero pressure. Subsequent thermal spike simulations are performed in constant volume and energy (*NVE*) with a thermostated region (at 600 K) at the y and z boundaries to model heat diffusion out of the system. The Berendsen thermostat[63] with a temperature damping parameter of 0.1 ps is employed at each of the 1-nm thick thermostat regions. Figures 1(a) and 1(b) show the time evolution of temperature as a function of radial distance from the centerline of a cylindrical thermal spike in a perfect UO_2 crystal subjected to a 4-nm radius spike with an energy of $S_{e,eff} = 16$ keV/nm, simulated using a standard box (60 supercells along y and z) compared to a larger box (100 supercells along y and z). The temperature profiles in both boxes as a function of time are similar, indicating that the thermostat setup is appropriate to simulate the heat diffusion out of the system.

The thermal spike approach approximates the effect of electronic stopping on the dynamics of atoms simulated in MD. The main advantage of this approach is that it considers only the effective energy transferred to the lattice. Therefore, uncertainties in the variables and approximations used in a more complex method such as a coupled 2T-MD method[64,65] are excluded. Intricacies in the coupled 2T-MD method can be found in Refs. 50, 64, and 65. In addition, performing coupled 2T-MD simulations for systems with millions of atoms remains extremely computationally expensive. Therefore, similar to the previous work of Huang *et al.* and Govers *et al.*, we employ the thermal spike approach. We note that even though the 2T model was used by Huang, it was decoupled from the MD simulations.

Huang *et al.* noted that after 1 ps, the MD temperature profile became smooth and similar to the profile from the 2T model. Govers used an initially uniform temperature profile but varied the radius of the thermal spike and noted that the evolution of the temperature profile beyond 1 ps was similar. Furthermore, Govers *et al.* noted that only limited re-solution can occur within the first several pico seconds and subsequently chose 4 nm as the thermal spike radius in their production runs. Even though the approach used by Govers is more approximate, it circumvents the uncertainties in the 2T model as used by Huang. Therefore, we follow the approach of Govers and co-workers and defer the more complex procedure for the future when full 2T-MD simulations become more reliable and practical. In our simulations, a thermal spike radius of 4 nm is chosen based on the electron-phonon interaction mean free path $\lambda = 4$ nm, which represents the effective length of heat diffusion in the electron-phonon coupled system obtained by Toulemonde *et al.*[50]

Each bubble is created by filling a spherical void with randomly distributed Xe atoms. Charge neutrality is imposed in creating the voids. Table I summarizes the bubbles explored in this study. For simplicity, a 0.8-nm radius bubble containing 36 Xe atoms is denoted as R0.8N36. The gas density in the bubbles ranges from 10.0 to 24.2 Xe/nm^3 (or 2.2 to 5.3 g/cm^3). Thermal spike energies of 10, 13, 16, 20, 25, and 30 keV/nm are investigated. With a 4-nm radius cylindrical thermal spike, a 10-keV/nm energy deposition corresponds to about 2.7 eV/atom. For comparison, the thermal energy at the melting point is equivalent to a kinetic energy of about 0.4 eV/atom.

An adaptive time step with a maximum atomic displacement of 0.025 Å per step is used in the simulations. Figure 1(c) shows the temperature evolution of systems subjected to different $S_{e,eff}$. The corresponding numbers of re-solved Xe from a representative R0.8N36 bubble are shown in Fig. 1(d). Following previous works,[35–37] re-solved atoms are defined as those beyond 1 nm from the bubble surface. The results show that re-solution occurs gradually over tens of pico seconds before it reaches steady-state. The time to reach the steady-state count of re-solved atoms varies from 10 ps for the $S_{e,eff} = 10$ keV/nm to 70 ps for the $S_{e,eff} = 30$ keV/nm. The simulations are followed until the system cools down below 700 K. This setup typically allows for a steady-state behavior to last for 50 ps, indicating that no significant changes are expected (within the MD time scale). As evident from Fig. 1(d), the re-solution evolution with 16 keV/nm spike reaches a steady-state behavior between 25 and 30 ps. The corresponding temperature profile [Fig. 1(a)] shows that at 30 ps, the hottest part of the spike region is still around 4000 K.

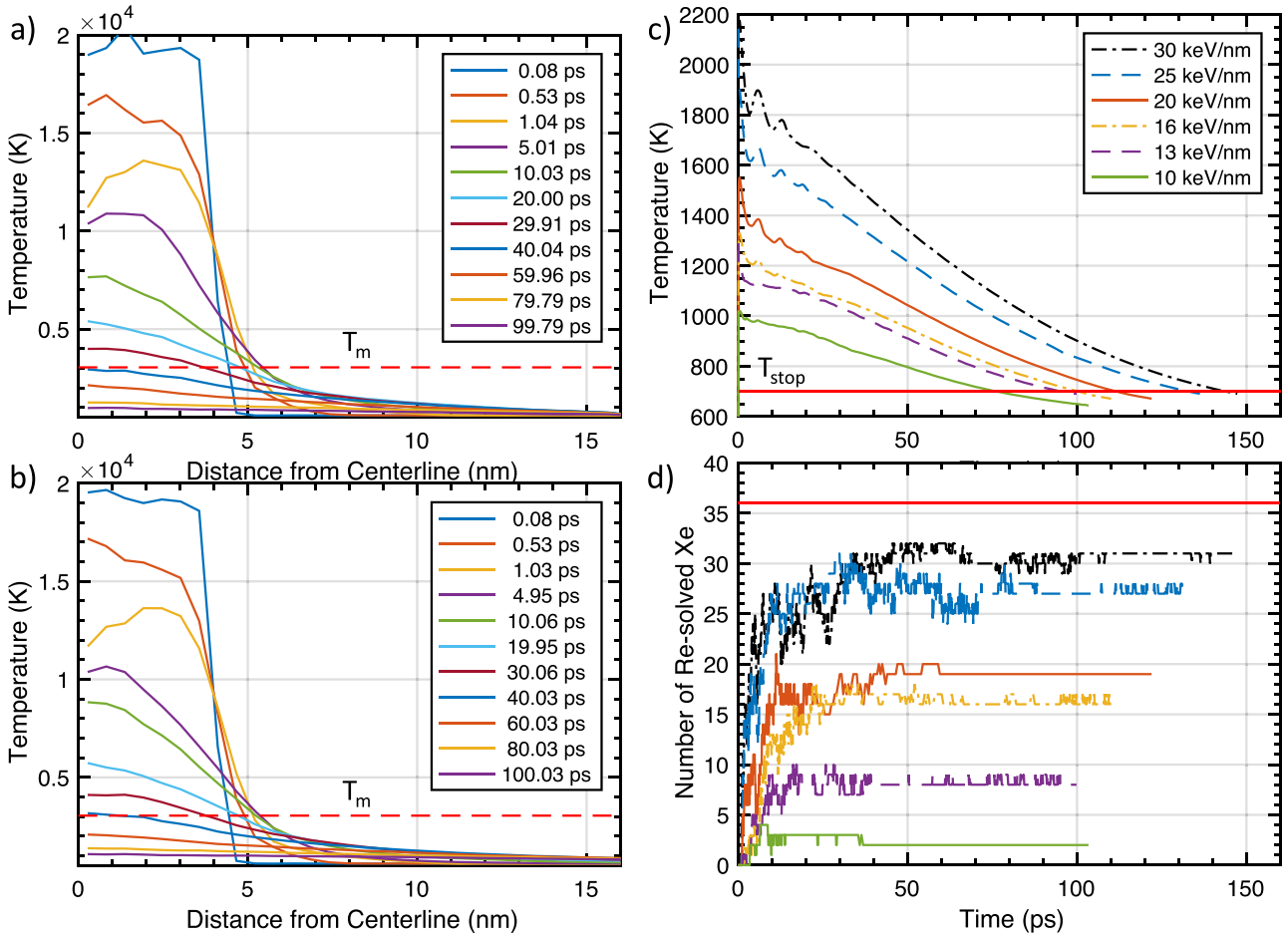

FIG. 1. Time evolution of the temperature profile as a function of radial distance from the centerline of a cylindrical thermal spike in a perfect UO_2 crystal subjected to a 4-nm radius spike with $S_{e,eff} = 16$ keV/nm simulated using (a) $10 \times 60 \times 60$ and (b) $10 \times 100 \times 100$ supercells. The horizontal line in (a) and (b) denotes the melting temperature calculated with the empirical potentials ($T_m = 3050$ K). Production runs with Xe bubbles are simulated with a $150 \times 60 \times 60$ supercell. (c) Temperature evolution of systems subjected to $S_{e,eff}$ from 10 to 30 keV/nm and (d) the corresponding re-solution from a representative R0.8N36 bubble. Horizontal line in (c) denotes the temperature below which the simulations are stopped ($T_{stop} = 700$ K). Horizontal line in (d) denotes the total number of Xe in the R0.8N36 bubble.

This result corroborates a previous study[22] of the effect of a 30-keV/nm thermal spike on Xe diffusion, which showed that the mean squared displacement of Xe within the thermal spike reaches a steady state once the temperature in the thermal spike region falls below 5000 K. Temperature in a nuclear fuel pellet varies depending on the location from the fuel centerline, with typical values ranging from 773 to about 1473 K. Since the thermal conductivity at 1473 K is lower than at 600 K, the thermal spike will last somewhat longer if the simulations are performed at 1473 K. The calculated thermal conductivity at 300, 1000, and 1500 K is approximately 14.6, 4.5, and 3.0 W/m/K, respectively.[57] Note that the decrease from 1000 K to 1500 K is small. Meanwhile, from the temperature profile, the temperature in regions close to the thermal spike (i.e., between 4 and 10 nm from the spike axis) already reaches >1000 K within 5 ps and remains >1000 K after 60 ps. This indicates that even though the system is initially at 600 K, the local temperature in regions surrounding the thermal spike is practically >1000 K throughout the duration of the simulation that is pertinent to re-solution. Therefore, we expect that the results presented in this study are applicable for other regions of fuel pellets, i.e., the temperature effect is small within the pellet temperature variation.

TABLE I. Setup of Xe bubbles: bubble radius (R), number of vacant sites (N_{vac}) given in UO_2 formula unit, number of Xe atoms (N), N/N_{vac}, gas density in the bubbles (ρ_{Xe}), and bubble pressure (P). ρ_{Xe} and P are obtained from MD simulations at 600 K and based on the void volume ($V_{void} = 0.25a^3N_{vac}$, where $a = 5.4854$ Å is the lattice constant at 600 K). Uncertainties in P denote the standard deviations calculated with five bubbles.

R (nm)	N_{vac} (UO_2)	N	N/N_{vac}	ρ_{Xe} (Xe/nm^3)	P (GPa)
0.6	23	10	0.43	10.5	1.1 ± 0.1
0.6	23	15	0.65	15.8	3.3 ± 0.1
0.6	23	20	0.87	21.1	7.0 ± 0.3
0.8	58	24	0.41	10.0	0.6 ± 0.1
0.8	58	36	0.62	15.0	2.3 ± 0.1
0.8	58	48	0.83	20.1	5.4 ± 0.1
1.5	369	369	1.00	24.2	7.5 ± 0.1
2.0	804	562	0.70	16.9	1.9 ± 0.1
3.0	2779	2779	1.00	24.2	6.5 ± 0.1

III. ON-CENTERED THERMAL SPIKE

In this section, we explore re-solution due to an on-centered thermal spike event. Figure 2 shows the number of

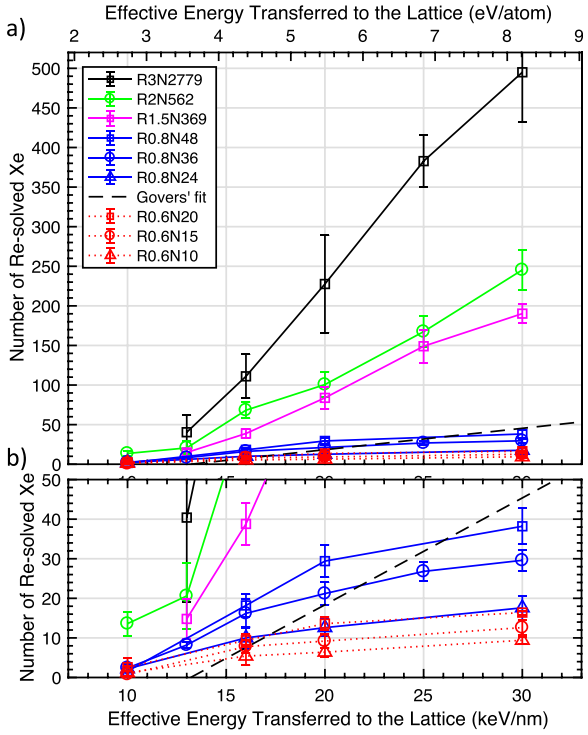

FIG. 2. (a) Number of re-solved Xe due to an on-centered thermal spike as a function of thermal spike energy. Data for the R0.6 and R0.8 bubbles are replotted in (b) for clarity. Error bars denote the standard deviations calculated from five bubbles. The dashed line is the linear fit from Govers *et al.*[37] [also given in Eq. (1)].

re-solved Xe as a function of the thermal spike energy. The empirical model from Govers *et al.* [see Eq. (1)] is superimposed for comparison. Evidently, more atoms are re-solved for larger bubbles, deviating from the universal fit by Govers. Only the data for the smaller bubbles (radius < 1 nm) are comparable with the results of Govers. The data for the larger bubbles are significantly larger than predicted by the model. Given that our simulation setup is the same as in Govers work, the different results for the larger bubbles are presumably due to the different properties of the interatomic potentials that govern the kinetics and thermodynamics of disordering and recrystallization in the system. For instance, because the Morelon potential predicts a higher melting temperature than the Cooper potential used in this study, the area of the melt within the thermal spike for the re-solution to occur will be smaller and hence a smaller re-solution. The effect of a smaller melt area is expected to be more pronounced for a larger bubble since the outer part of the bubble will be closer to the periphery of the melt where the temperature is lower than the core of the melt. While this hypothesis may partly explain why the re-solution obtained by Govers *et al.* is smaller than our study as the bubble size increases, future studies are needed to fully assess the differences in both potentials including the different Xe-U and Xe-O interactions used in our study compared to Govers *et al.*, which may affect Xe diffusion within the melt and re-solution.

The effect of gas density on re-solution is studied using the R0.6 and R0.8 bubbles. Three different densities are explored ranging from approximately 10 to 21 Xe/nm^3 (see Table I for details). For both bubble sizes, more atoms are re-solved for higher gas densities. However, the fraction of re-solved Xe with respect to the number of Xe in the bubble does not appear to depend on the density as shown in Fig. 3. The fraction of re-solved Xe is directly related to the probability of a Xe atom (averaged over the Xe atoms in the bubble) to be re-solved. Therefore, the results suggest that the re-solution probability does not depend on gas density. For this reason, the data for different gas densities are simply averaged for subsequent analyses.

Figure 4(a) shows the overall results for the fraction of re-solved Xe (χ) for various bubble sizes as a function of thermal spike energy. Opposite to the number of re-solved Xe, for a given thermal spike energy, χ is smaller for larger bubbles. This indicates that Xe in a larger bubble has a lower probability to be re-solved. This behavior is expected since a Xe atom in the interior of a larger bubble has a lower chance to be re-solved. Analogously, higher thermal spike energies are needed to fully re-solve larger bubbles. From this observation, an exponentially saturating function is employed to model re-solution as a function of the thermal spike energy $S_{e,eff}$

$$\chi_0 = 1 - e^{-\alpha(S_{e,eff} - S_{e,c})}, \tag{2}$$

where α is the saturation factor that depends on bubble radius and $S_{e,c}$ is the critical energy as previously defined in Eq. (1).

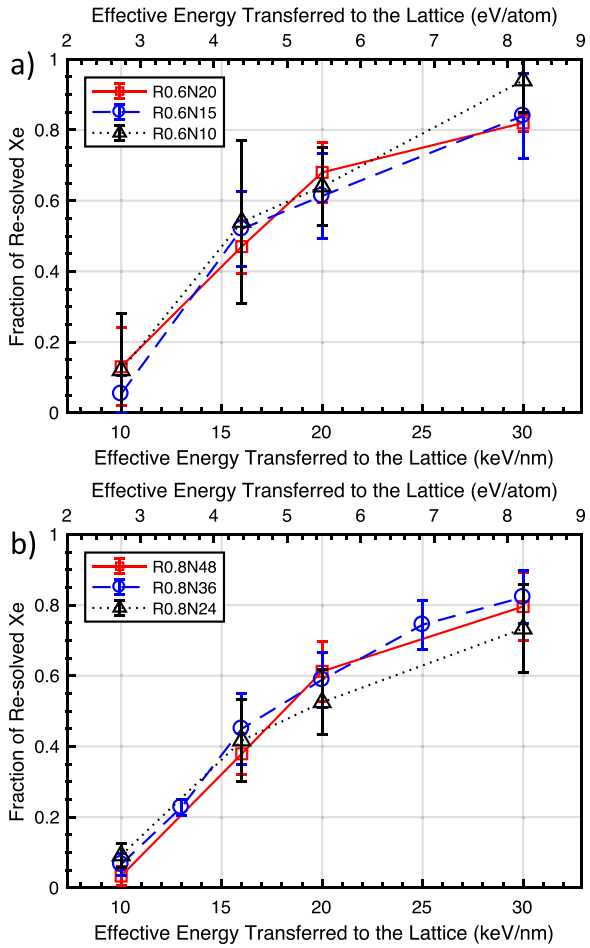

FIG. 3. Fraction of re-solved Xe due to an on-centered thermal spike as a function of thermal spike energy for bubbles with radii (a) 0.6 nm and (b) 0.8 nm. Error bars denote the standard deviations calculated from five bubbles.

The subscript in χ_0 indicates that this χ is due to an on-centered spike. Furthermore, we assume that $S_{e,c}$ is invariant of the bubble radius; therefore, data for different bubble radii are fit concurrently. The critical energy is found to be $S_{e,c} = 9.04$ keV/nm (or 2.47 eV/atom). The saturation factor is plotted as a function of the bubble radius in Fig. 4(b). A simple inverse power function appears to adequately describe the radius dependence of the saturation factor. The fitting results are presented in Fig. 4 and the on-centered thermal spike re-solution model becomes

$$\chi_0 = 1 - e^{-0.05(S_{e,eff} - 9.04)/R^{1.47}}, \tag{3}$$

where $S_{e,eff}$ is in keV/nm and R in nm.

IV. OFF-CENTERED THERMAL SPIKE

The effect of an off-centered thermal spike is studied by shifting the axis of the spike away from the centerline of the bubbles. R0.8N36, R2N562, and R3N2779 bubbles are used to explore the size dependence of the off-centered effect. These sizes represent the small, medium, and large bubbles within the range of sizes used in our simulations. Preliminary simulations with the R0.8N36 bubbles using $S_{e,eff} = 10$ keV/nm show that the re-solution is too limited, particularly as the off-centered distance is increased, to yield reliable statistics with five bubbles. Subsequently, $S_{e,eff} = 16$ keV/nm is chosen. This energy corresponds to the estimated thermal spike energy by Govers *et al.* where dislocation loops and disoriented nanodomains start to form as previously mentioned. Therefore, 16 keV/nm is a reasonable choice to get significant enough re-solution within the practical range of thermal spike energies for our purposes.

Figure 5 shows the plots of χ as a function of off-centered distance (r) for different bubble radii. χ decreases nonlinearly with r showing a trend that is reminiscent of a Gaussian distribution. For all bubble sizes, χ becomes practically zero at a critical off-centered distance $r_c = R + R_{spike}$. From this observation, the data points are fitted with a generalized Gaussian function with the data points (0, χ_0) and (r_c, 0) used as constraints

$$\chi = \chi_0 e^{-br^c} - y_1[e^r - 1]e^{-r_c},$$
$$y_1 = \chi_0 e^{-b(r_c)^c}/(1 - e^{-r_c}), \tag{4}$$

where b and c are the fitting parameters. For $r > r_c$, $\chi = 0$. The fitted models are shown and summarized in Fig. 5. To better compare the curves from different bubble radii, we normalize the data and plot the normalized fraction of re-solved Xe (χ/χ_0) as a function of normalized off-centered distance (r/r_c) in Fig. 6. The normalized plots appear to fall into one curve within the standard deviations of the data. Therefore, to simplify, the normalized data are combined and fitted with a single curve. The off-centered thermal spike re-solution model thus becomes

$$\chi/\chi_0 = e^{-3.09(r/r_c)^{1.76}} - y_1[e^{(r/r_c)} - 1]e^{-1},$$
$$y_1 = e^{-3.09}/(1 - e^{-1}). \tag{5}$$

As in Eq. (4), the model is only defined up to $r = r_c$; hence, it is understood that for $r > r_c$, $\chi = 0$.

V. RE-SOLUTION RATE

Equations (3) and (5) constitute a model of the fraction of re-solved Xe (χ) from a bubble of radius R as a function of $S_{e,eff}$ and r. In turn, $S_{e,eff}$ decreases as the ionizing fission product travels through the material. Let us consider a cylindrical coordinate system with the origin at the bubble center and the axial direction x oriented along the fission track. A fission can occur randomly at any (x, r) coordinate. Therefore, the re-solution rate can be calculated as a volume integral of the product between χ and fission rate density (i.e., the number of fissions per volume per second, $\dot{F}$)

$$b_{het} = \sum_{i=1}^{2} \int_{r=0}^{\infty} \int_{x=0}^{\infty} \chi_i \dot{F} 2\pi r dr dx, \tag{6}$$

where the subscript in b_{het} indicates that this is a heterogeneous re-solution rate. The index i denotes the species of the fission products, which runs from 1 to 2 corresponding to two fission products per fission, thereby ignoring the relatively small fraction of ternary fission events. The x dependence of χ is embedded in $S_{e,eff}$ since the electronic stopping power decreases with distance. The current model of the resolution rate that is commonly used assumes that any bubbles within the thermal spike interaction volume are completely re-solved and the two fission products are of the same species

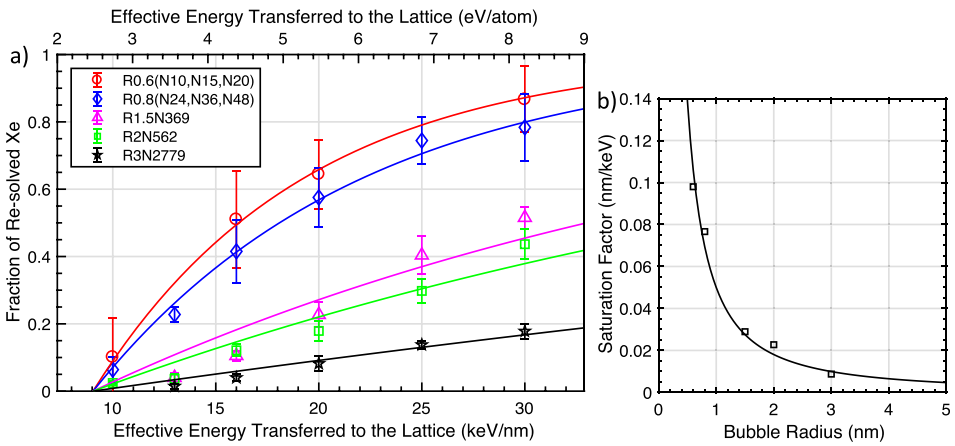

FIG. 4. (a) Fraction of re-solved Xe due to an on-centered thermal spike (χ_0) as a function of thermal spike energy. Error bars denote the standard deviations calculated from 15 bubbles for the R0.6 and R0.8 nm radius bubbles and five bubbles for the larger bubbles. Data are fitted using an exponentially saturating function $\chi_0 = 1 - e^{-\alpha(S_{e,eff} - S_{e,c})}$ where $S_{e,c} = 9.04$keV/nm (or 2.47eV/atom) and the saturating factor $\alpha = 0.05/R^{1.47}$ is plotted in b).

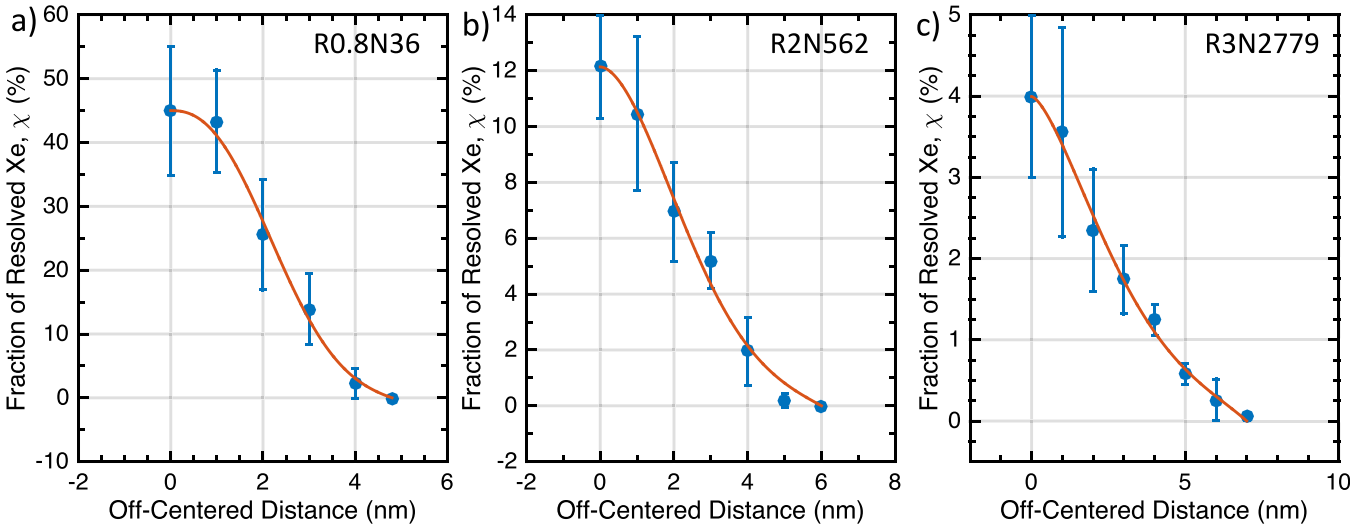

FIG. 5. Fraction of re-solved Xe due to an off-centered thermal spike as a function of the off-centered distance obtained using a 16-keV/nm thermal spike. Error bars denote the standard deviations from five bubbles. Data are fitted using $\chi = \chi_0 e^{-br^c} - y_1[e^r - 1]e^{-r_c}$, where $y_1 = \chi_0 e^{-b(r_c)^c}/(1 - e^{-r_c})$ and χ_0 is 0.45, 0.12, and 0.04 for R0.8N36, R2N562, and R3N2779 bubbles, respectively, and $r_c = R + R_{spike}$. The fitted values are $b = 0.09$ and $c = 2.41$ (R0.8N36), $b = 0.14$ and $c = 1.80$ (R2N562), and $b = 0.16$ and $c = 1.50$ (R3N2779).

$$b_{het} = 2\dot{F}\pi r_c^2 \mu, \tag{7}$$

where $r_c = R + R_{spike}$ and μ is the stopping range of the fission products. Using Eqs. (3), (5), and (6), an updated model can be constructed. By recognizing that the r and x dependencies of χ in Eq. (6) are separable through Eq. (5) for r and Eq. (3) for x, Eq. (6) can now be written as

$$b_{het} = \dot{F}\sum_{i=1}^{2}\int_{r=0}^{\infty}\left(\frac{\chi_i}{\chi_{0,i}}\right)2\pi r dr \int_{x=0}^{\infty}\chi_{0,i}dx. \tag{8}$$

Using Eq. (5), the r integration can be readily calculated as

$$\int_{r=0}^{\infty}\left(\frac{\chi_i}{\chi_{0,i}}\right)2\pi r dr \approx 0.25\pi r_c^2, \tag{9}$$

and the overall model becomes

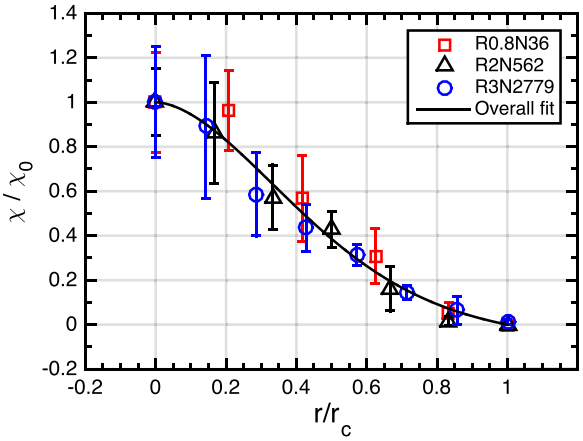

FIG. 6. Normalized fraction of re-solved Xe (χ/χ_0) as a function of normalized off-centered distance (r/r_c) where $r_c = R + R_{spike}$. Data are obtained with $S_{e,eff} = 16$ keV/nm. Error bars denote the standard deviations from five bubbles. The fit curve is $\chi/\chi_0 = e^{-b(r/r_c)^c} - y_1[e^{(r/r_c)} - 1]e^{-1}$, where $y_1 = e^{-b}/(1 - e^{-1})$, with $b = 3.09$ and $c = 1.76$.

$$b_{het} = 0.25\pi r_c^2 \dot{F}\sum_{i=1}^{2}\int_{x=0}^{\mu_{c,i}}\left[1 - e^{-0.05(S_{e,eff,i} - 9.04)/R^{1.47}}\right]dx, \tag{10}$$

where $S_{e,eff,i}$ is the effective electronic stopping power of fission product-i and where the upper limit of the integration has been replaced with the critical range of fission product-i ($\mu_{c,i}$) at which $S_{e,eff,i}$ (at $x = \mu_{c,i}$) = 9.04 keV/nm since there is no re-solution beyond $\mu_{c,i}$.

To evaluate the re-solution rate model for a given R and $\dot{F}$, we need to know the fission product (FP) yields and the kinetic energy distribution of the fission products. Fission product yields depend on the fissioning nuclide and the energy of the neutron causing the fission. Here, we evaluate the model for fission from $^{235}_{92}$U due to thermal neutrons (neutron energy = 0.0253 eV), which is applicable for light-water reactors (LWRs). An independent fission product yield (iFPY) denotes the distribution of fission products produced directly from the fission prior to any radioactive decay. Many fission products are short-lived and form large decay chains of radio-nuclides. Fission products are neutron-rich and typically decay along an isobar by β^- emission. A cumulative fission product yield (cFPY) denotes the distribution of fission products at the end of the decay chains. Therefore, cFPY is linked to the iFPY through the decay schemes. cFPY can be readily counted experimentally. On the other hand, iFPY is calculated using semi-empirical models[66–69] that are fitted to give sums over fission product decay chains that are consistent with the measured values for cFPY.

Evidently, the distribution of fission products continuously changes throughout the decay chains. To determine which yield (iFPY or cFPY) is more appropriate for evaluating the re-solution rate, we take insights from the following. The cumulative yields are produced by decays with a half-life of $\tau_{1/2} > 1$ ms.[70] In a binary fission (producing a pair of light and heavy FPs, e.g., Kr and Ba), the total kinetic energy is distributed between the FPs according to their inverse masses

(due to conservation of total momentum); hence, the light FP exhibits a higher stopping power (more contribution to the re-solution). Consider a typical light FP of Kr-90 with a kinetic energy of 101.5 MeV (will be shown later). Such an isotope has an initial relativistic speed of $0.05c$ (c is the speed of light) $= 1.5 \times 10^7$ m/s. As will be shown later, the range of this isotope is about 8 μm. Even though the slowing down is non-linear, the isotope would stop well before the half-life. Therefore, iFPY is more appropriate for our purpose.

The iFPY from the JEFF-3.3[1,71,72] and ENDF/B-VI[1,66] databases is considered. Note that the fission yields for U-235 in the current ENDF/B-VIII.0 are still the same as in version VI, which is based on the seminal work of England and Rider in 1993.[66] The databases contain detailed iFPY for each atomic mass (A), charge (atomic number Z), and isomeric state. Typically, for a given Z, the yield distribution is centered around the most probable isotope (isotope with the highest yield). Therefore, to simplify the calculation of $S_{e,eff}$ of various fission products, the total iFPY (sum over isotopes) is taken for each element and the mass of the most probable isotope is taken as the atomic mass.

Figure 7 shows the iFPYs as a function of Z obtained from both databases. Note that the sum of iFPY over all elements in Fig. 7 is 2 corresponding to two fission products per fission. The iFPY plot from the JEFF database is symmetric (the yields of the light FPs are the same as those of their corresponding heavy FPs), while the plot from the ENDF database is not. For binary fissions, a symmetric iFPY is expected. Analysis of why the iFPY from ENDF is not symmetric is beyond the scope of this paper. Subsequently, we take the iFPY from the JEFF database in which the iFPY for U-235 is also more recently evaluated (updated) than ENDF. Nevertheless, the discrepancies between the two iFPYs are very small and either iFPY would result in practically the same re-solution rate. Most of the iFPY distribution is contained within 18 elements as labelled in Fig. 7. The sum of the iFPY of these 18 elements is 1.96 (JEFF) and 1.95 (ENDF). These are the elements that are considered in the evaluation of the re-solution rate.

As previously mentioned, for each element, the mass of the most probable isotope is taken as the atomic mass. Using this mass, the kinetic energy for each element is obtained from the experimental data of kinetic energy as a function of fission product mass taken from Ref. 73 as compiled in the EXFOR database (*dataset 23014005*).[74] Table II summarizes the list of these isotopes and their corresponding kinetic energies. Subsequently, ion irradiations are simulated using the SRIM code[75] to obtain the electronic stopping power decay as a function of distance of these isotopes in UO_2. For each isotope, 1000 simulations are performed for averaging. Figure 8 shows plots of the total electronic stopping power (S_e) as a function of distance obtained from the SRIM simulations along with the fit curves.

Knowing the fission yields, the re-solution rate model [Eq. (10)] becomes

$$b_{het} = 0.25\pi r_c^2 \dot{F} \sum_i y_i \int_{x=0}^{\mu_{c,i}} \left[1 - e^{-0.05(\zeta S_{e,i} - 9.04)/R^{1.47}}\right] dx, \quad (11)$$

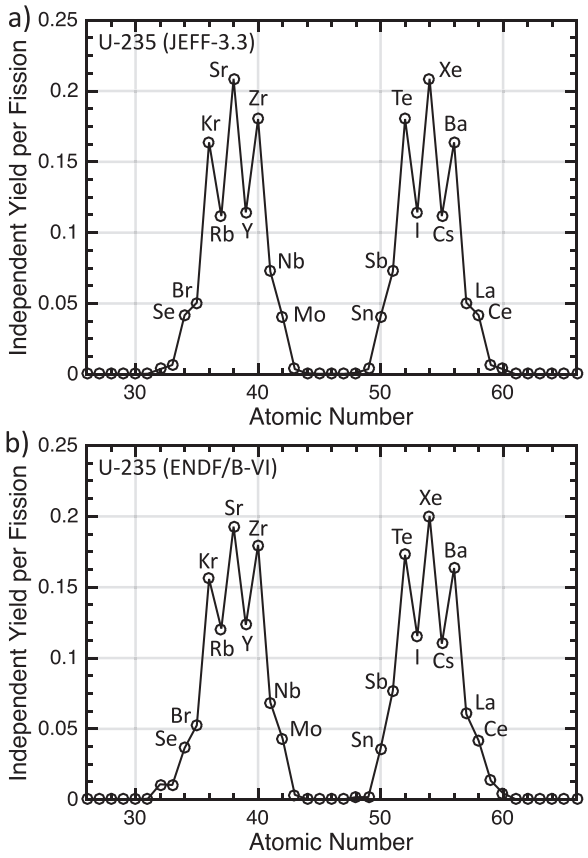

FIG. 7. Independent fission product yield summed over isotopes as a function of atomic number from the fission of U-235 with 0.0253-eV neutrons, as plotted from the (a) JEFF-3.3 [1, 71, 72] database and (b) ENDF/B-VI[1,66] database.

where y_i is the iFPY of fission product-i and the sum is over all fission products. Note that the effective electronic stopping power in Eq. (11) has been explicitly expressed as ζS_e. Using iFPY shown in Fig. 7 and S_e as a function of x shown in Fig. 8, we evaluate b_{het} for several values of ζ from 0.5 to 0.9. Figure 9 shows the re-solution rate as a function of Xe bubble radius for a typical fission rate density of 10^{-8}/nm^3 s. Govers *et al.* estimated ζ from 0.73 to 0.89 based on the onset thermal spike energy (16 keV/nm) for the formation of dislocation loops. The 0.73 value is obtained if the loops are

TABLE II. List of the most probable isotopes of the 18 light and heavy fission products (FPs) with the largest total independent fission yields from the fission of U-235 with 0.0253-eV neutrons obtained from the JEFF-3.3 database.[1,71,72] The kinetic energy (*KE*) is obtained from EXFOR database (*dataset 23014005*).[73,74]

Light FP	*KE* (MeV)	Heavy FP	*KE* (MeV)
$^{86}_{34}$Se	101.3	$^{148}_{58}$Ce	60.2
$^{87}_{35}$Br	101.2	$^{146}_{57}$La	62.6
$^{90}_{36}$Kr	101.5	$^{144}_{56}$Ba	64.8
$^{93}_{37}$Rb	101.2	$^{141}_{55}$Cs	68.2
$^{94}_{38}$Sr	101.1	$^{138}_{54}$Xe	71.9
$^{97}_{39}$Y	101.3	$^{136}_{53}$I	74.6
$^{100}_{40}$Zr	101.4	$^{134}_{52}$Te	77.5
$^{102}_{41}$Nb	101.8	$^{133}_{51}$Sb	78.8
$^{104}_{42}$Mo	101.2	$^{130}_{50}$Sn	81.5

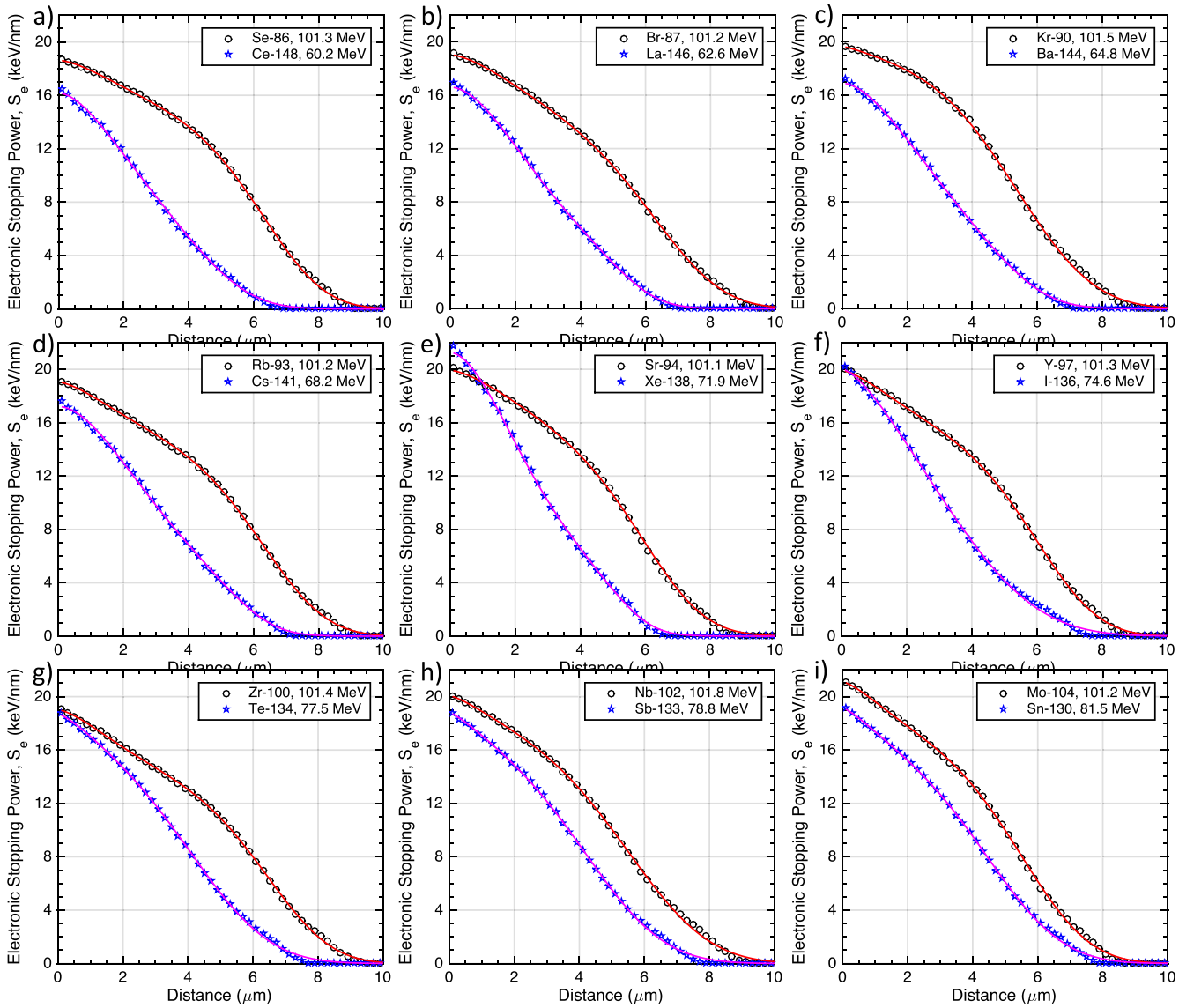

FIG. 8. Total electronic stopping power (S_e) of various fission products in UO_2 calculated with the SRIM code as a function of distance traveled by the fission products measured from the location of the fission reactions that produce these fission products. Each panel contains each pair of light and heavy fission products produced in a binary fission reaction. The fit curves are as follows (y denoting S_e in keV/nm and x denoting distance traveled in μm): Se: $y = 14.09\exp(-0.000192x^{4.481}) + 4.54\exp(-0.1875x^{1.587})$, Ce: $y = 7.69\exp(-0.004155x^{3.481}) + 8.49\exp(-0.2045x^{1.765})$; Br: $y = 12.97\exp(-0.000346x^{4.139}) + 6.05\exp(-0.1505x^{1.621})$, La: $y = 4.84\exp(-0.000236x^{4.931}) + 11.76\exp(-0.1285x^{1.857})$; Kr: $y = 17.32\exp(-0.002529x^{3.324}) + 2.32\exp(-0.3537x^{1.332})$, Ba: $y = 6.64\exp(-0.001559x^{3.903}) + 10.26\exp(-0.1449x^{1.809})$; Rb: $y = 13.89\exp(-0.000245x^{4.348}) + 5.15\exp(-0.2172x^{1.535})$, Cs: $y = 5.27\exp(-0.000214x^{4.882}) + 11.94\exp(-0.1193x^{1.858})$; Sr: $y = 13.11\exp(-0.000298x^{4.354}) + 6.80\exp(-0.1405x^{1.571})$, Xe: $y = 5.06\exp(-0.000110x^{5.438}) + 16.20\exp(-0.1536x^{1.806})$; Y: $y = 14.39\exp(-0.000350x^{4.258}) + 5.52\exp(-0.2355x^{1.518})$, I: $y = 11.08\exp(-0.017360x^{2.582}) + 8.94\exp(-0.2472x^{1.515})$; Zr: $y = 13.25\exp(-0.000188x^{4.433}) + 5.76\exp(-0.2274x^{1.513})$, Te: $y = 13.21\exp(-0.008047x^{2.973}) + 5.49\exp(-0.3396x^{1.375})$; Nb: $y = 15.55\exp(-0.002155x^{3.343}) + 4.52\exp(-0.2900x^{1.374})$, Sb: $y = 13.80\exp(-0.008101x^{2.959}) + 5.00\exp(-0.3864x^{1.320})$; and Mo: $y = 15.72\exp(-0.001096x^{3.776}) + 5.38\exp(-0.3189x^{1.425})$, Sn: $y = 5.34\exp(-0.382600x^{1.32}) + 13.81\exp(-0.0055x^{3.129})$.

formed by the thermal spike of the light FPs, while the 0.89 value is from the heavy FPs. Experimental measurements are needed to discern which FPs are responsible for the loop formation, which to our knowledge are currently absent. In the meantime, the 0.73 value represents a conservative estimate since light FPs exhibit higher stopping power and hence are more likely to form the dislocation loops than the heavy FPs. Therefore, the curve for $\zeta = 0.73$ is considered and compared with published re-solution rates.

As evident from Fig. 9, the re-solution rate with $\zeta = 0.73$ varies as a function of bubble radius from 3.7, 2.5, 1.9, 1.3, 1.0, 0.8, and 0.7×10^{-4}/s for bubble radius of 0.5, 0.75, 1, 1.5, 2, 3, and 4 nm, respectively. The rate is practically 0.5×10^{-4}/s for $R > 4.5$ nm. Turnbull,[33] Veshchunov,[76,77] and Lösönen[4,7] developed various models of bubble evolution and compared the bubble distribution to experimental data to empirically fit the re-solution rate in their models. Turnbull estimated an empirical value between 0.26 and 1.2×10^{-4}/s for bubble radius of about 5 nm. Veshchunov obtained an upper limit of re-solution rate of 3.2×10^{-4}/s for 0.5–0.6 nm radius bubbles, in excellent agreement with our model. Lösönen estimated a value of 2 to 4×10^{-4}/s (independent of bubble radius). These empirical values are fairly consistent with our model with $\zeta = 0.73$. Turnbull's lower

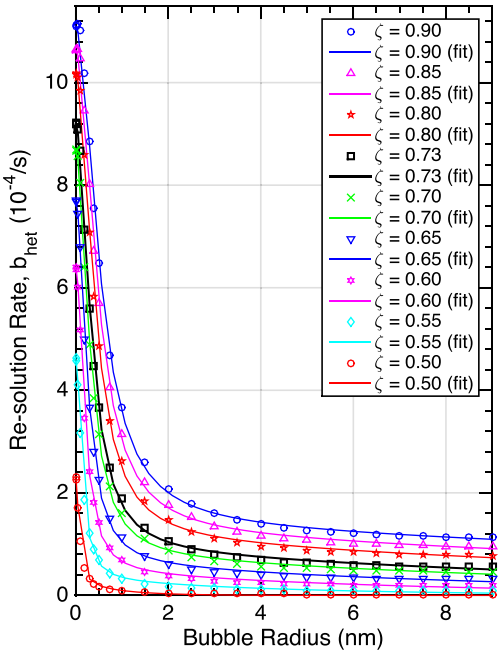

FIG. 9. Evaluated Xe re-solution rates as a function Xe bubble radius for several values of the ratio between the thermal spike energy and the total electronic stopping power ($\zeta = S_{e,eff}/S_e$) for fission rate density of 10^{-8}/nm^3 s. Plots are ordered with the topmost curve corresponding to the largest ζ. Data points are the evaluated values obtained by numerically integrating Eq. (11). Smooth curves are fit curves given in Table III.

limit of 0.26×10^{-4}/s for $R = 5$ nm suggests that $\zeta > 0.6$. On the other hand, Veshchunov's upper limit of 3.2×10^{-4}/s for 0.5–0.6 nm radius bubbles suggests $\zeta < 0.8$. Therefore, $\zeta = 0.73$ is a reasonable value for our model.

VI. CONCLUSIONS

Analyses based on a systematic set of MD thermal spike simulations reveal trends in the re-solution probability as a function of bubble radius (R), thermal spike energy (ζS_e), and off-centered distance (r) between the thermal spike axis and the bubble center. The trends allow construction of a new re-solution rate model to be parametrized in terms of these variables. The off-centered effect is shown to decrease the re-solution by a factor of 0.25 (averaged over the circular cross-section of the thermal spike). The dependence on the thermal spike energy shows that no-resolution occurs for $\zeta S_e < 9.04$ keV/nm. Evaluation of the re-solution rate model has been presented using a distribution of U-235 fission products due to thermal neutrons. The decay of the total electronic stopping power (S_e) for each fission product over distance is simulated and taken into account. For a typical fission rate density of 10^{-8}/nm^3/s, the re-solution rate is then calculated as a function of R for several values of ζ. Comparison with published empirical values suggests that $\zeta = 0.73$ is a reasonable choice. Using this value, all empirically fit rates are consistent with the model developed here. The results also support the notion that a thermal spike is the rate-controlling process for Xe gas bubble re-solution in UO_2[33] as opposed to collision cascades.

TABLE III. The evaluated Xe re-solution rates for fission rate density of 10^{-8}/nm^3 s as plotted in Fig. 9 are fit with $y(x) = a_1 \exp(-b_1 x) + (y(0) - a_1)/(1 + cx^2) \exp(-b_2 x^2)$, where x is the Xe bubble radius (nm) and y is the re-solution rate. $y(0)$ denotes the asymptotic value at $x = 0$.

ζ	$y(0)$ (10^{-4}/s)	a_1 (10^{-4}/s)	b_1 (1/nm)	b_2 (1/nm)	c (1/nm^2)
0.90	11.0851	1.5052	0.0362	0.0203	3.4123
0.85	10.6297	1.3479	0.0438	0.0241	4.2214
0.80	10.1521	1.1986	0.0546	0.0299	5.4612
0.73	9.1816	0.949	0.0703	0.0371	7.982
0.70	8.6745	0.8401	0.0792	0.0407	9.6585
0.65	7.6984	0.6721	0.1028	0.0526	14.272
0.60	6.3925	0.5025	0.1411	0.0727	23.1967
0.55	4.6175	0.3433	0.2284	0.1276	45.6624
0.50	2.3061	0.2786	1.1008	1.605	150.6689

ACKNOWLEDGMENTS

This research was supported by the U. S. Department of Energy (DOE), Office of Nuclear Energy (NE), Office of Science (SC), and Office of Advanced Scientific Computing Research (ASCR) through the Scientific Discovery through Advanced Computing (SciDAC) project on Fission Gas Behavior. This research used resources of the Argonne Leadership Computing Facility, which is a DOE Office of Science User Facility supported under Contract No. DE-AC02-06CH11357, as well as the PNNL Institutional Computing at Pacific Northwest National Laboratory.

[1]See www-nds.iaea.org/endf for "ENDF Database."
[2]M. Tonks, D. Andersson, R. Devanathan, R. Dubourg, A. El-Azab, M. Freyss, F. Iglesias, K. Kulacsy, G. Pastore, S. R. Phillpot, and M. Welland, J. Nucl. Mater. **504**, 300 (2018).
[3]J. H. Shea, J. Nucl. Mater. **501**, 302 (2018).
[4]P. Lösönen, J. Nucl. Mater. **496**, 140 (2017).
[5]G. Pastore, L. P. Swiler, J. D. Hales, S. R. Novascone, D. M. Perez, B. W. Spencer, L. Luzzi, P. Van Uffelen, and R. L. Williamson, J. Nucl. Mater. **456**, 398 (2015).
[6]G. Pastore, L. Luzzi, V. D. Marcello, and P. V. Uffelen, Nucl. Eng. Des. **256**, 75 (2013).
[7]P. Lösönen, J. Nucl. Mater. **304**, 29 (2002).
[8]P. Lösönen, J. Nucl. Mater. **280**, 56 (2000).
[9]R. J. White and M. O. Tucker, J. Nucl. Mater. **118**, 1 (1983).
[10]P. Chakraborty, M. R. Tonks, and G. Pastore, J. Nucl. Mater. **452**, 95 (2014).
[11]P. Garcia, G. Martin, C. Sabathier, G. Carlot, A. Michel, P. Martin, B. Dorado, M. Freyss, M. Bertolus, R. Skorek, J. Noirot, L. Noirot, O. Kaitasov, and S. Maillard, Nucl. Instrum. Methods Phys. Res., Sect. B **277**, 98 (2012).
[12]G. Brillant, F. Gupta, and A. Pasturel, J. Nucl. Mater. **412**, 170 (2011).
[13]A. Chartier, L. Van Brutzel, and M. Freyss, Phys. Rev. B **81**, 174111 (2010).
[14]H. Y. Geng, Y. Chen, Y. Kaneta, M. Kinoshita, and Q. Wu, Phys. Rev. B **82**, 094106 (2010).
[15]P. Garcia, P. Martin, G. Carlot, E. Castelier, M. Ripert, C. Sabathier, C. Valot, F. DÁcapito, J. L. Hazemann, O. Proux, and V. Nassif, J. Nucl. Mater. **352**, 136 (2006).
[16]A. Jelea, R. J. M. Pellenq, and F. Ribeiro, J. Nucl. Mater. **444**, 153 (2014).
[17]J.-Y. Oh, Y.-H. Koo, J.-S. Cheon, B.-H. Lee, and D.-S. Sohn, J. Nucl. Mater. **372**, 89 (2008).
[18]A. D. Whapham, Nucl. Appl. **2**, 123 (1966).
[19]J. A. Turnbull, C. A. Friskney, J. R. Findlay, F. A. Johnson, and A. J. Walter, J. Nucl. Mater. **107**, 168 (1982).
[20]K. Nogita and K. Une, Nucl. Instrum. Methods Phys. Res., Sect. B **141**, 481 (1998).
[21]K. Nogita and K. Une, J. Nucl. Mater. **250**, 244 (1997).
[22]M. W. D. Cooper, C. R. Stanek, J. A. Turnbull, B. P. Uberuaga, and D. A. Andersson, J. Nucl. Mater. **481**, 125 (2016).

[23]D. A. Andersson, P. Garcia, X. Y. Liu, G. Pastore, M. Tonks, P. Millett, B. Dorado, D. R. Gaston, D. Andrs, R. L. Williamson, R. C. Martineau, B. P. Uberuaga, and C. R. Stanek, J. Nucl. Mater. **451**, 225 (2014).
[24]D. A. Andersson, B. P. Uberuaga, P. V. Nerikar, C. Unal, and C. R. Stanek, Phys. Rev. B **84**, 054105 (2011).
[25]X. Y. Liu, B. P. Uberuaga, D. A. Andersson, C. R. Stanek, and K. E. Sickafus, Appl. Phys. Lett. **98**, 151902 (2011).
[26]K. Govers, S. E. Lemehov, and M. Verwerft, J. Nucl. Mater. **405**, 252 (2010).
[27]K. Govers, S. Lemehov, and M. Verwerft, J. Nucl. Mater. **374**, 461 (2008).
[28]A. E. Thompson and C. Wolverton, Phys. Rev. B **87**, 104105 (2013).
[29]H. J. Matzke, Radiat. Eff. **53**, 219 (1980).
[30]G. T. Lawrence, J. Nucl. Mater. **71**, 195 (1978).
[31]R. J. White, J. Nucl. Mater. **325**, 61 (2004).
[32]R. S. Nelson, J. Nucl. Mater. **31**, 153 (1969).
[33]J. A. Turnbull and R. M. Cornell, J. Nucl. Mater. **36**, 161 (1970).
[34]D. R. Olander and D. Wongsawaeng, J. Nucl. Mater. **354**, 94 (2006).
[35]D. Schwen, M. Huang, P. Bellon, and R. S. Averback, J. Nucl. Mater. **392**, 35 (2009).
[36]M. Huang, D. Schwen, and R. S. Averback, J. Nucl. Mater. **399**, 175 (2010).
[37]K. Govers, C. L. Bishop, D. C. Parfitt, S. E. Lemehov, M. Verwerft, and R. W. Grimes, J. Nucl. Mater. **420**, 282 (2012).
[38]D. C. Parfitt and R. W. Grimes, J. Nucl. Mater. **392**, 28 (2009).
[39]M. V. Speight, Nucl. Sci. Eng. **37**, 180 (1969).
[40]K. Forsberg and A. R. Massih, J. Nucl. Mater. **135**, 140 (1985).
[41]K. Forsberg and A. R. Massih, J. Nucl. Mater. **127**, 141 (1985).
[42]K. Forsberg and A. R. Massih, Modell. Simul. Mater. Sci. Eng. **15**, 335 (2007).
[43]R. L. Williamson, J. D. Hales, S. R. Novascone, M. R. Tonks, D. R. Gaston, C. J. Permann, D. Andrs, and R. C. Martineau, J. Nucl. Mater. **423**, 149 (2012).
[44]M. S. Veshchunov, A. V. Boldyrev, A. V. Kuznetsov, V. D. Ozrin, M. S. Seryi, V. E. Shestak, V. I. Tarasov, G. E. Norman, A. Y. Kuksin, V. V. Pisarev, D. E. Smirnova, S. V. Starikov, V. V. Stegailov, and A. V. Yanilkin, Nucl. Eng. Des. **295**, 116 (2015).
[45]B. Michel, C. Nonon, J. Sercombe, F. Michel, and V. Marelle, Nucl. Technol. **182**, 124 (2013).
[46]R. S. Nelson, J. Nucl. Mater. **25**, 227 (1968).
[47]J. A. Turnbull, J. Nucl. Mater. **38**, 203 (1971).
[48]H. R. Faust, Eur. Phys. J. A **14**, 459 (2002).
[49]M. Toulemonde, E. Paumier, and C. Dufour, Radiat. Eff. Defects Solids **126**, 201 (1993).
[50]M. Toulemonde, C. Dufour, A. Meftah, and E. Paumier, Nucl. Instrum. Methods Phys. Res., Sect. B **166**, 903 (2000).
[51]T. Wiss, H. Matzke, C. Trautmann, M. Toulemonde, and S. Klaumünzer, Nucl. Instrum. Methods Phys. Res., Sect. B **122**, 583 (1997).
[52]J. Soullard, J. Nucl. Mater. **78**, 125 (1978).
[53]M. W. D. Cooper, M. J. D. Rushton, and R. W. Grimes, J. Phys.: Condens. Matter **26**, 105401 (2014).
[54]D. Manara, C. Ronchi, M. Sheindlin, M. Lewis, and M. Brykin, J. Nucl. Mater. **342**, 148 (2005).
[55]N. D. Morelon, D. Ghaleb, J. M. Delaye, and L. Van Brutzel, Philos. Mag. **83**, 1533 (2003).
[56]K. Govers, S. Lemehov, M. Hou, and M. Verwerft, J. Nucl. Mater. **376**, 66 (2008).
[57]M. J. Qin, M. W. D. Cooper, E. Y. Kuo, M. J. D. Rushton, R. W. Grimes, G. R. Lumpkin, and S. C. Middleburgh, J. Phys.: Condens. Matter **26**, 495401 (2014).
[58]M. W. D. Cooper, S. T. Murphy, P. C. M. Fossati, M. J. D. Rushton, and R. W. Grimes, Proc. R. Soc., A **470**, 0427 (2014).
[59]M. W. D. Cooper, S. T. Murphy, M. J. D. Rushton, and R. W. Grimes, J. Nucl. Mater. **461**, 206 (2015).
[60]M. W. D. Cooper, N. Kuganathan, P. A. Burr, M. J. D. Rushton, R. W. Grimes, C. R. Stanek, and D. A. Andersson, J. Phys.: Condens. Matter **28**, 405401 (2016).
[61]K. T. Tang and J. P. Toennies, J. Chem. Phys. **118**, 4976 (2003).
[62]S. Plimpton, J. Comput. Phys. **117**, 1 (1995).
[63]H. J. C. Berendsen, J. P. M. Postma, W. F. van Gunsteren, A. DiNola, and J. R. Haak, J. Chem. Phys. **81**, 3684 (1984).
[64]D. M. Duffy and A. M. Rutherford, J. Phys.: Condens. Matter **19**, 016207 (2007).
[65]A. M. Rutherford and D. M. Duffy, J. Phys.: Condens. Matter **19**, 496201 (2007).
[66]T. England and B. Rider, "Evaluation and compilation of fission product yields 1993," Report No. LA-SUB-94-170; ON: DE95003450; TRN: 95:000123, 1995.
[67]A. C. Wahl, At. Data Nucl. Data Tables **39**, 1 (1988).
[68]A. C. Wahl, J. Radioanal. Chem. **55**, 111 (1980).
[69]A. C. Wahl, R. L. Ferguson, D. R. Nethaway, D. E. Troutner, and K. Wolfsberg, Phys. Rev. **126**, 1112 (1962).
[70]M. T. Pigni, M. W. Francis, and I. C. Gauld, Nucl. Data Sheets **123**, 231 (2015).
[71]R. W. Mills, "Fission product yield evaluation," Ph.D. thesis (University of Birmingham, UK, 1995).
[72]R. W. Mills, EPJ Web Conf. **146**, 04008 (2017).
[73]H. Baba, T. Saito, N. Takahashi, A. Yokoyama, T. Miyauchi, S. Mori, D. Yano, T. Hakoda, K. Takamiya, K. Nakanishi, and Y. Nakagome, J. Nucl. Sci. Technol. **34**, 871 (1997).
[74]See www-nds.iaea.org/exfor for "EXFOR Database."
[75]J. F. Ziegler, M. D. Ziegler, and J. P. Biersack, Nucl. Instrum. Methods Phys. Res., Sect. B **268**, 1818 (2010).
[76]M. S. Veshchunov, J. Nucl. Mater. **277**, 67 (2000).
[77]M. S. Veshchunov and V. I. Tarasov, J. Nucl. Mater. **437**, 250 (2013).